ACS central science

Research Article

http://pubs.acs.org/journal/acscii

Extraction of Lanthanide and Actinide Ions from Aqueous Mixtures Using a Carboxylic Acid-Functionalized Porous Aromatic Framework

Selvan Demir,[†,‡,§] Nicholas K. Brune,[†,‡,§] Jeffrey F. Van Humbeck,[†,∥] Jarad A. Mason,[†] Tatiana V. Plakhova,[‡,⊥] Shuao Wang,[†,‡,#] Guoxin Tian,[‡,¶] Stefan G. Minasian,[‡] Tolek Tyliszczak,[○] Tsuyoshi Yaita,[∞] Tohru Kobayashi,[∞] Stepan N. Kalmykov,[⊥] Hideaki Shiwaku,[∞] David K. Shuh,[‡] and Jeffrey R. Long[*,†,△,▽]

[†]Department of Chemistry and [△]Department of Chemical and Biomolecular Engineering, University of California, Berkeley, California 94720, United States

[‡]Chemical Sciences Division, [▽]Materials Sciences Division, and [○]Advanced Light Source, Lawrence Berkeley National Laboratory, Berkeley, California 94720, United States

[⊥]Chemistry Department, Lomonosov Moscow State University, Leninskie Gory, Moscow 11991, Russia

[∞]Actinide Chemistry Group, Energy and Environment Science Division, Quantum Beam Science Center, Japan Atomic Energy Agency, 1-1-1 Kouto, Sayo-cho, Sayo-gun, Hyogo 679-5148, Japan

[¶]Radiochemistry Department, China Institute of Atomic Energy, Beijing 102413, China

Supporting Information

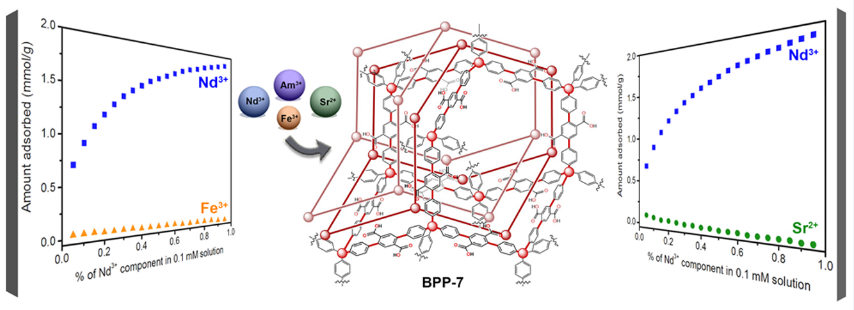

ABSTRACT: Porous aromatic frameworks (PAFs) incorporating a high concentration of acid functional groups possess characteristics that are promising for use in separating lanthanide and actinide metal ions, as required in the treatment of radioactive waste. These materials have been shown to be indefinitely stable to concentrated acids and bases, potentially allowing for multiple adsorption/stripping cycles. Additionally, the PAFs combine exceptional features from MOFs and inorganic/activated carbons giving rise to tunable pore surfaces and maximum chemical stability. Herein, we present a study of the adsorption of selected metal ions, Sr^{2+}, Fe^{3+}, Nd^{3+}, and Am^{3+}, from aqueous solutions employing a carbon-based porous aromatic framework, BPP-7 (Berkeley Porous Polymer-7). This material displays high metal loading capacities together with excellent adsorption selectivity for neodymium over strontium based on Langmuir adsorption isotherms and ideal adsorbed solution theory (IAST) calculations. Based in part upon X-ray absorption spectroscopy studies, the stronger adsorption of neodymium is attributed to multiple metal ion and binding site interactions resulting from the densely functionalized and highly interpenetrated structure of BPP-7. Recyclability and combustibility experiments demonstrate that multiple adsorption/stripping cycles can be completed with minimal degradation of the polymer adsorption capacity.

INTRODUCTION

The fission and neutron capture reactions occurring in nuclear reactors generate a waste stream of more than 40 elements, which includes the entirety of the periodic table from germanium to erbium, in addition to the transuranic elements from neptunium to curium.[1] Additionally, the unavoidable corrosion of stainless steel structural elements delivers numerous first row transition metals.[2] Effective conversion of such a complex and highly radioactive mixture into waste forms suitable for long-term storage, along with recovering and reprocessing fissile uranium and plutonium, demands the separation of this mixture into separate groups (Figure 1, FP, fission products; MA, minor actinides).[3] Initial separation of uranium and plutonium for reprocessing is accomplished by the PUREX (plutonium uranium redox extraction) process,[4] which can be modified to include coextraction of neptunium (Figure 1, separation A).[5] Of the elements remaining in the raffinate,

Received: March 6, 2016
Published: April 12, 2016

DOI: 10.1021/acscentsci.6b00066
ACS Cent. Sci. 2016, 2, 253−265

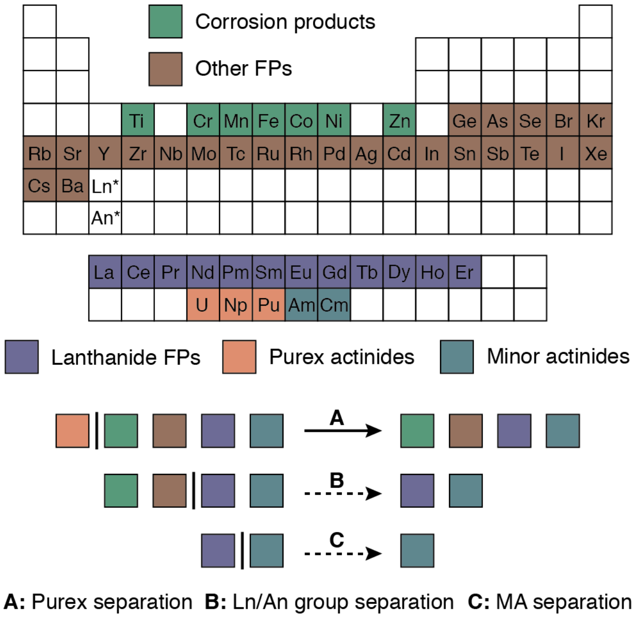

Figure 1. Separation of fission products (FPs) including highly radioactive PUREX actinides and minor actinides (MA).

the minor actinides—especially americium—dominate the long-term radiotoxicity and heat load of spent fuels.[6,7] Provided they can be isolated in sufficient purity, such species could be recycled and utilized for energy production or transmuted into alternative isotopes that would shorten waste storage time-frames.

Complete purification of the minor actinides requires the development of two selective separations.[3] First, the lanthanide fission products must be partitioned together with the minor actinides in a process known as group separation (Figure 1, separation B). For this, biphasic solvent extraction using chelating diamides[8,9] (i.e., the diamide extraction or DIAMEX process) or carbamoylphosphine oxides[10,11] (i.e., the trans-uranic extraction or TRUEX process) represents the current state of the art. The group separation is required to provide solutions containing exclusively lanthanide and actinide ions, so that the increased strength of the actinide−ligand interaction can subsequently be exploited for selective extraction of the minor actinides (Figure 1, separation C). Soft ligand sets such as triazinylpyridines[12] and alkylated thiophosphates[13] have demonstrated promising efficiencies in separating actinides from lanthanides, but these ligands would be rendered inoperable by the presence of transition metal impurities.

Importantly, none of these processes have been successfully demonstrated or utilized beyond a laboratory scale. As is true for the PUREX process, solvent extractions will generate large volumes of organic waste via hydrolytic and radiolytic degradation of the solvents and extractants. In addition, the equipment required for multistage extraction and stripping, such as mixer-settlers and centrifugal contactors, greatly increases capital costs. An alternative approach—solid-phase extraction—has been pursued by impregnating the pores of macroporous polymer substrates with extractant solutions.[14] Such methods have received considerable attention because they eliminate the agitated contactors demanded by solvent extraction, while maintaining the binding selectivity of conventional ligand sets. In addition, nanoparticles and mesoporous materials have been tested for the encapsulation of early actinides.[15−17] However, the stability of these composite materials against radiation damage and acid hydrolysis is questionable due to the weak noncovalent interaction between the extractants and porous substrates. It has recently been shown that high acid concentration, heat, and γ-radiation all result in loss of extractants from substrates, with concomitant reduction in extraction capacity and separation efficiency.[18,19] In addition, concerns about generating secondary solid wastes that are difficult to degrade—and so, must *themselves* be disposed of—may also hinder the industrial adoption of solid-phase extraction processes.

The development of porous adsorbents densely furnished with selective binding sites appended through covalent bonds could provide materials with both unprecedented separation performance and adequate stability in these extremely challenging conditions. However, the most widely investigated microporous materials face specific limitations for lanthanide group separation (Figure 2). Metal−organic frameworks (MOFs), which have displayed noteworthy performance in gas-phase separation, storage, sensing, and catalysis applications,[20−27] generally do not possess the hydrolytic stability necessary for long-term application in highly acidic solutions (Figure 2). A zirconium-based MOF has recently displayed promising UO_2^{2+} adsorption from mildly acidic (pH = 2.5) solution, though further investigations on this material showed some sensitivity to more vigorous conditions involving dissolution in 0.1 M H_3PO_4/DMSO.[28] Conversely, traditional adsorbents such as zeolites and activated carbons, while extremely robust, cannot be fine-tuned with the myriad reactions available from synthetic organic chemistry. Addition-

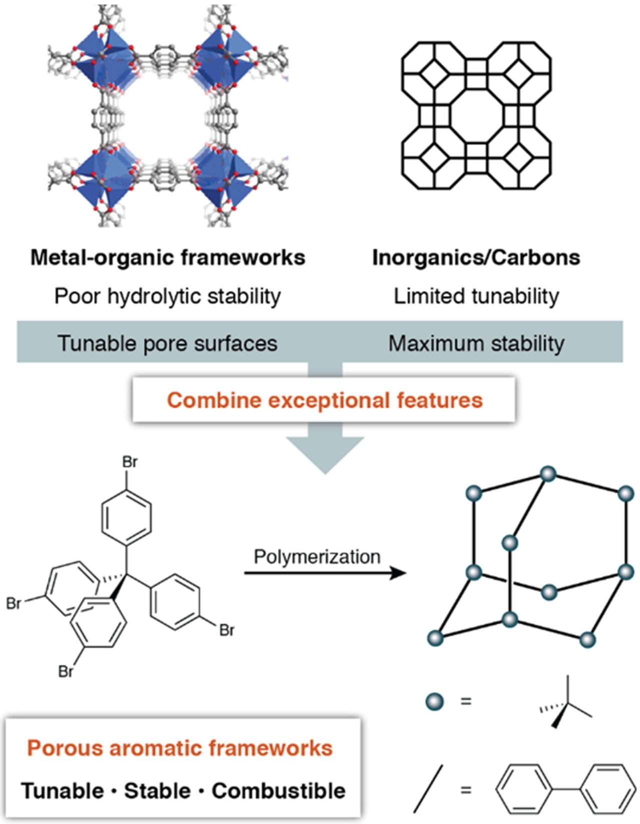

Figure 2. Potential advantages of porous aromatic frameworks (PAFs) for challenging adsorptions.

ally, the inability of purely inorganic or MOF supports to be completely converted to volatile products by combustion would generate a large volume of secondary radiological waste.

Preliminary studies performed on densely functionalized porous aromatic frameworks (PAFs)[29] present clear advantages over both microporous materials and solid-phase extraction composites. First, these materials have been demonstrated to be indefinitely stable to concentrated acids (e.g., 6 M HCl, 99% $ClSO_3H$) and bases (e.g., 6 M KOH),[30−32] potentially allowing for multiple adsorption/stripping cycles. Second, like MOFs, the more chemically stable PAFs are amenable to targeted surface functionalization using synthetic organic chemistry, either before or after framework assembly.

Recently, we reported catalytic routes to different porous aromatic polymers densely functionalized with carboxylic acids, together with a demonstration of their utility in ammonia capture.[33] Among these, the framework BPP-7, which can be readily prepared through polymerization of 1-nonyl terephthalate ester followed by side chain cleavage, showed a remarkable NH_3 uptake performance. This material features carboxylic acid lined pores ranging from ∼6.0 to 6.5 Å in diameter and a BET surface area of 705 m^2/g, which are indicative of a multifold[34] interpenetrated structure (Figure 3).

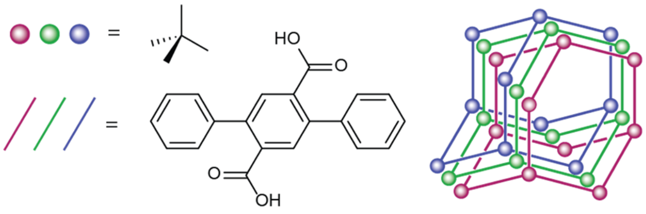

Figure 3. Multifold interpenetrated structure of BPP-7.

To obtain a high adsorption capacity for the extraction of metal ions from a low-concentration solution, a large enthalpy of adsorption[35] (ΔH_{ads}) is necessary, which can be achieved by promoting multiple chemical interactions between the metal ion and the binding site. BPP-7 was chosen as a densely functionalized PAF with a great potential for cooperative binding as a result of its highly interpenetrated structure. Its relatively larger pore size compared to other interpenetrated PAFs further allowed for improved uptake kinetics in ammonia adsorption.[33] BPP-7 features binding sites with numerous carboxylic acid groups and is an excellent candidate for lanthanide and actinide group separation given that these ions are notoriously oxophilic.

Herein, we report the utilization of the densely functionalized PAF BPP-7 for metal ion separation, an approach to simultaneously address the need for separation selectivity, adsorption capacity, hydrolytic stability, and combustibility demanded by a real-world lanthanide/actinide group separation.

RESULTS AND DISCUSSION

Metal Ion Adsorption Isotherms and Langmuir Fitting. The uptake of metal ions by BPP-7 was measured at various concentration ranges for neodymium(III) (2.76×10^{-6} mM to 2.52 mM), iron(III) (0.113 mM to 4.33 mM), and strontium(II) (2.17×10^{-3} mM to 2.44 mM). As an initial investigation, the Nd^{3+}, Fe^{3+}, and Sr^{2+} ions were chosen as representative ions for group separation of the corrosion products, other fission products, and lanthanide fission products, respectively. The Fe^{3+} ion was chosen due to its high concentration in nuclear waste streams as a result of the corrosion of steel.[2] Strontium-90 is environmentally toxic, and is an intermediate activity waste product.[36] The Nd^{3+} ion was chosen as a midsize lanthanide ion.

The adsorption isotherms for Nd^{3+}, Fe^{3+}, and Sr^{2+} uptake were fitted with Langmuir models (Table 1), and the fits agree to within 4% of the measured values, which is within the experimental error (Figure 4). While a single-site Langmuir equation could be used to describe the Fe^{3+} adsorption isotherm, dual-site Langmuir equations were necessary for Nd^{3+} and Sr^{2+}. Modeling the adsorption sites for Nd^{3+} and Sr^{2+} required including both a strong and a weak adsorption site, while the Fe^{3+} data could be modeled with only one weak site. Thus, the Fe^{3+} weak site interactions represent an average binding against which the Nd^{3+} and Sr^{2+} binding can be compared. There is evidence provided by Extended X-ray Absorption Fine Structure (EXAFS) data (see EXAFS section for more detail) that the strong adsorption site for Nd^{3+} and Sr^{2+} likely involves interactions with multiple carboxylate groups. Presumably, the larger ionic radii of Nd^{3+} and Sr^{2+} allow for such interactions, as opposed to a smaller Fe^{3+} ion.

Table 1. Single- and Dual-Site Langmuir Fit Parameters for Single-Component Adsorption Isotherms[a]

	Nd^{3+}	Sr^{2+}	Fe^{3+}
$n_{sat,1}$	0.43	0.39	7.7
b_1	97350	278	0.26
$n_{sat,2}$	1.9	2.6	
b_2	34.8	0.59	

[a] Units for n are mmol/g, and units for b are mM^{-1}.

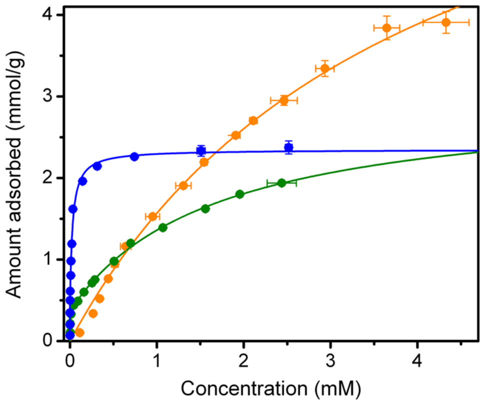

Figure 4. Room temperature Nd^{3+} (blue), Sr^{2+} (green), Fe^{3+} (orange) ion adsorption characteristics of BPP-7.

In Table 1, the b_1 and b_2 Langmuir parameters represent the affinities of the metal ion for the binding sites. Since Fe^{3+} is modeled with a single weak site interaction, only a b_1 parameter was calculated. The Nd^{3+} and Sr^{2+} data were fitted with two b parameters, with b_1 as the strong site interaction and b_2 as the weak site interaction. Notably, the b_1 parameter for Nd^{3+} (97350 mM^{-1}) is orders of magnitude greater than those of Sr^{2+} (278 mM^{-1}) and Fe^{3+} (0.26 mM^{-1}) ions, which suggests that adsorption of Nd^{3+} is much stronger than Sr^{2+} and Fe^{3+} adsorption. Indeed, this can be observed in the relative steepness of the adsorption isotherms at low concentrations (Figure 4). The near vertical steepness of the Nd^{3+} adsorption isotherm indicates that Nd^{3+} binds the framework most strongly, followed by Sr^{2+} and Fe^{3+}. While Nd^{3+} has the highest uptake at low concentrations, Fe^{3+} has the highest uptake at saturation owing to its smaller size. One would expect the uptake saturation to be inversely related to ionic radii, and since Nd^{3+} and Sr^{2+} have nearly equivalent ionic radii, their saturation capacities are similar and much lower than that of Fe^{3+}. The $n_{sat,1}$ and $n_{sat,2}$ parameters measure the saturation capacities (mmol/g) of the two adsorption sites. For both Nd^{3+} and Sr^{2+}, the saturation capacity of the stronger binding site is lower, which is expected. The relation of all Langmuir b_1 parameters indicates that overall Nd^{3+} ions interact with one site more strongly than Sr^{2+} or Fe^{3+} ions. Presumably, this can be ascribed to the greater charge density of Nd^{3+} relative to Sr^{2+} and the larger ionic radius relative to Fe^{3+}, which provides a better match for certain rigid binding pockets within BPP-7 involving multiple carboxylate/carboxylic acid groups.

Another important feature to note is that the adsorption capacity of Nd^{3+} within BPP-7 approaches 2.5 mmol/g, which is much higher than the uptake of lanthanides in similarly functionalized materials used for actinide uptake, such as the family of phosphoric acid functionalized silicas (exhibiting a maximum Eu uptake of 0.38 mmol/g).[37] The large uptake capacity and multisite interactions result from a very high density of active sites and large overall surface area (705 m^2/g), which in turn arises from the highly interpenetrated structure of BPP-7.[33] Minor deviations from the proposed single- and dual-site Langmuir models may be attributed to electrostatic repulsion between adsorbed metal ions, which would reduce the binding affinity, resulting in occupation of fewer active sites than those available in the framework.[38]

IAST Calculations. Since binary adsorption isotherms are difficult to measure, it is often necessary to use an adsorption model such as ideal adsorbed solution theory (IAST) to predict mixture behavior from experimentally determined single-component isotherms.[39] The IAST method has been well established for metal ion uptake[40,41] and for a variety of adsorbents, including zeolites[42,43] and metal−organic frameworks.[44,45] The details of the IAST evaluation of selectivities, adsorbed quantities, and mixture purities for Nd^{3+}, Fe^{3+}, and Sr^{2+} are reported in the Experimental Section. IAST calculations were performed using the appropriate single- and dual-site Langmuir isotherm fits (Table 1).

Since the relative concentrations of isotopes of Nd^{3+}, Fe^{3+}, and Sr^{2+} ions can fluctuate in a radioactive waste stream,[46] IAST selectivities were calculated over a wide range of compositions for total concentrations of 0.1 and 1 mM. At both concentrations, BPP-7 exhibits a high selectivity for Nd^{3+} over Sr^{2+} and Fe^{3+}, with a more pronounced effect for the 0.1 mM mixtures (Figure 5). Importantly, selectivity for Nd^{3+} is most desired, since this ion is often used as an analogue for Am^{3+}, and shares similar physical and chemical properties with other lanthanides and actinides.[47] The relationship between Nd^{3+} and Am^{3+} uptake is explored further by experimentation below.

At all concentrations and compositions investigated, BPP-7 exhibits a high selectivity for Nd^{3+} over Fe^{3+} and Sr^{2+} and a moderate selectivity for Sr^{2+} over Fe^{3+}. For instance, for a solution containing just 5% Nd and 95% Fe or Sr, BBP-7 will selectively adsorb Nd with an IAST selectivity of 350 and 130, respectively, assuming a total concentration of 0.1 mM. IAST selectivity is also higher for Sr^{2+} than Fe^{3+}. Higher Nd^{3+} and Sr^{2+} selectivities at lower concentration can be attributed to the larger ionic radii for these ions, which presumably facilitates the simultaneous interaction with multiple carboxylic acid/carboxylate groups. The selectivity for Sr^{2+} over Fe^{3+} is also particularly important, in view of the environmentally hazardous nature of Sr-90.[36] Many contaminated sites where Sr^{2+} is present also contain large quantities of iron and other transition metals,[2] making this type of separation ideal for remediation purposes.

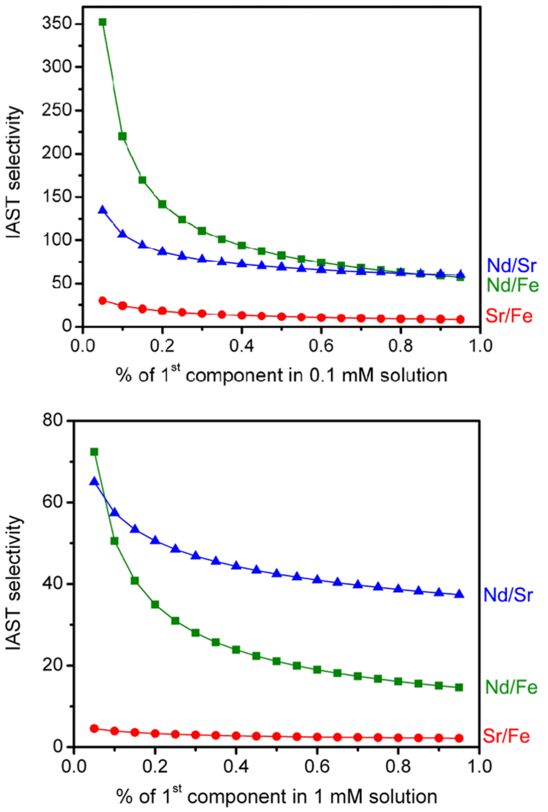

Figure 5. Ideal adsorbed solution theory (IAST) selectivities for 0.1 mM (top) and 1 mM (bottom) mixtures of Nd^{3+}/Sr^{2+} (blue triangles), Nd^{3+}/Fe^{3+} (green squares), and Sr^{2+}/Fe^{3+} (red circles) ions at rt.

IAST purity predictions listed in Figure 6 further illustrate the effectiveness of metal ion selectivity in BPP-7, as they suggest that Nd^{3+} can be isolated from Sr^{2+} and Fe^{3+} solutions at very high purity, reaching 99.6% purity over Fe^{3+} at a composition of 0.95% Nd^{3+} in a 1 mM mixture. Even at very low percent composition, Nd^{3+} shows an adsorbed phase that is 75% pure. This effect is even more pronounced for the 0.1 mM mixture, where the purity of Nd^{3+} rapidly surpasses 90%. High purity separations are also predicted for Sr^{2+} in competition with Fe^{3+}, for 0.6% composition in Sr and higher. This suggests that the coordination environment and strength of the metal ion−framework interactions are very uniform, and preferential binding is relatively consistent across all sites.

Additional IAST calculations were performed to evaluate the exact amounts of metal ion adsorbed from two-component mixtures at 0.1 and 1.0 mM concentrations. Figure S1 shows the results of the analysis for a binary mixture containing Nd^{3+} and Fe^{3+}. IAST adsorption for binary mixtures of Nd^{3+}/Sr^{2+} and Sr^{2+}/Fe^{3+} are presented in Figures S2 and S3. As expected, the adsorbed quantities were directly in line with IAST purities and selectivities, where the adsorption of Nd^{3+} is significantly higher in comparison to Sr^{2+} or Fe^{3+}.

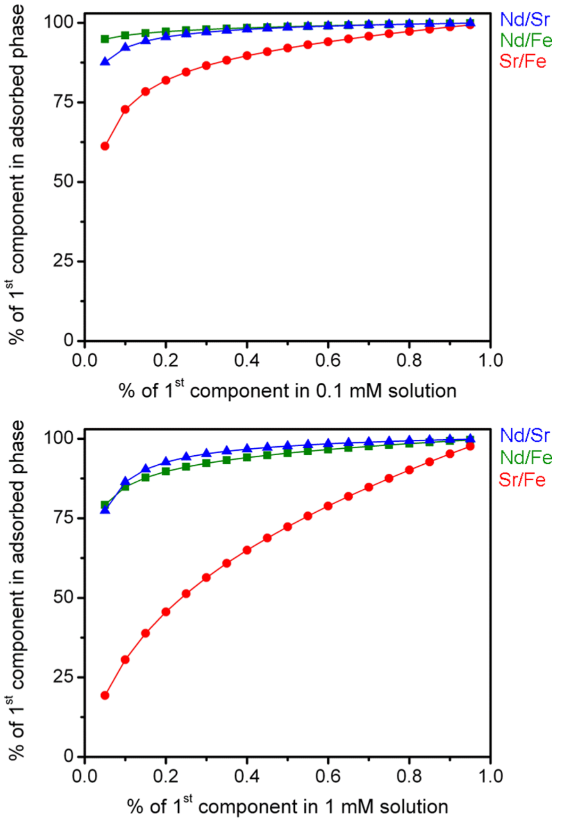

Figure 6. Ideal adsorbed solution theory (IAST) purities for 0.1 mM (top) and 1 mM (bottom) mixtures of Nd^{3+}/Sr^{2+} (green squares), Nd^{3+}/Fe^{3+} (blue triangles), and Sr^{2+}/Fe^{3+} (red circles) ions.

XAFS Measurements. The X-ray Absorption Near Edge Structure (XANES) spectra confirm the trivalent nature of Nd in the Nd-BPP-7 materials by comparison with Nd^{3+} in aqueous solution (see Figure S4). The edge-jump obtained from the near-edge spectra confirms the original Nd concentration in Nd-BBP-7 to be ~20 wt %. No radiation damage was observed from the response at the Nd K-edge during the course of the X-ray Absorption Fine Structure (XAFS) experiments.

The EXAFS function, $k^3\chi(k)$, and the Fourier transform magnitude, $FT(k^3\chi(k))$, of Nd-BPP-7 are shown in Figure 7. The fits to the spectra were performed based on the interpretation of two-shell models for the largest first (~2.0 Å) and second (~2.5 Å) peaks in the FT using metrical parameters obtained from previous studies of similar systems.[48,49] According to proton replacement reactions (see below), two protons are lost per complexed Nd atom, which infers that two carboxylate groups are likely involved in the PAF coordination of Nd; therefore, on average two carboxylate groups provide coordination sites, in which a carboxylate oxygen atom contributes to form a part of the first coordination shell. Accordingly, Figure 7 shows the EXAFS data with the corresponding two-shell fits, which are superior to single-shell fits. The conceptual model for the fits considers the possibility of Nd interactions with oxygen atoms from carboxylate and carboxylic acid groups, as well as guest water molecules, for the first peak; Nd interactions with the secondary, noncoordinating carbon and oxygen atoms of the carboxylate and carboxylic acid groups, and potentially carbon atoms from the interpenetrating PAF network, form the second peak. The first shell fit incorporates the knowledge that there will be distances characteristic of Nd–O(carboxylate/carboxylic acid) and Nd–O(water) ligation, as mentioned previously. Interactions with hydroxide under the experimental conditions, like the possibility of Cl^- coordination, are unlikely and would be difficult to resolve in the experiment (see Figure S4 for a schematic of possible interactions). There is no apparent multiple scattering peak in Figure 7, indicating that, if there is bidentate coordination by carboxylate groups, it is distorted and/or disordered. The initial distances obtained from EXAFS fitting (Table 2, Figure S5) suggest that carboxylate groups may coordinate to Nd in a monodentate fashion, and the resulting bond angle of Nd–O–C is less than 150°, since the focusing effect derived from a three-atom linear arrangement is also absent in this coordination mode. However, the large degree of

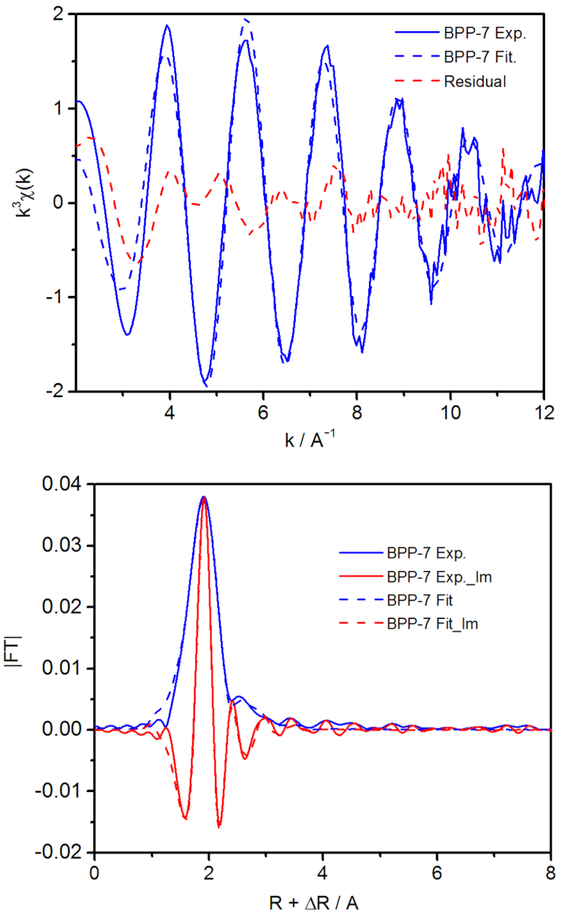

Figure 7. EXAFS function $k^3\chi(k)$ and the two-shell fitting results for the Nd-BPP-7 (top) and Fourier transform magnitudes $[FT(k^3(k))]$ and two-shell fitting curves for the Nd-BPP-7 (bottom). The imaginary components are shown in red traces.

Table 2. Structural Parameters Obtained from the Two-Shell Nd K-Edge EXAFS Analysis[a]

	S_0^2	N	R/Å	σ^2/Å^2	E_0/eV	Res./%
Nd–O(1) (Lig., H_2O)	0.9	9	2.483 ± 0.003	0.009	4.8	3.6
Nd···O(2) (Lig.) Nd···C (Lig.)	0.9	10	3.310 ± 0.009	0.019	4.8	3.6

[a] The error in R was determined as 2σ by fitting. Lig. = BPP-7 ligand.

disorder and broadening within the first shell supports that there may be more than a single interaction mode for coordination.

A summary of the metric parameters obtained from the curve fitting results for the two-shell fit are summarized in Table 2. In this model, the Nd−O(1) distances are ~2.48 Å; the bond angle of Nd−O−C is less than 150°, while the second shell with surrounding carboxylate oxygens and multiple network carbons (Nd···O(2) and Nd···C) are detected at ~3.31 Å, together with a relatively large Debye−Waller factor (DWF). The large DWF includes disorder resulting from the various conformations of BPP-7 coordinating to the Nd^{3+} ions. As shown in Figure S4 and corresponding to known distances, the Nd−O(1) distance corresponds to an average of all Nd−carboxyl interactions.[50−52] The Nd−O(1) coordination number was determined to be ~9 during the fitting process, and the best fit was found with this value. This value agrees with the general Nd coordination number of 9, derived from the interactions with oxygen, which corresponds well to the known coordination number of Nd^{3+} in solutions and solids. It is clear that the interpenetrating nature of the BPP-7 materials leads to Nd bonding with more than one carboxylate unit identified in the first shell (O(1)), based on the coordination number of the second shell. Further details of the exact, detailed coordination environment of Nd with respect to oxygen are not readily discernible, as a result of the degree of disorder exhibited by Nd-BPP-7, the average environments yielded by EXAFS, and the coordination number error of ±25%. It is, however, clear that several water molecules are included in the first coordination sphere of Nd. The possibility of a charge-compensating perchlorate in a higher coordination shell further provides for the proper charge balance for the reaction.

Scanning Transmission X-ray Microscope (STXM) Measurements. STXM is a powerful tool for characterizing materials of biological, environmental, extraterrestrial, or synthetic origins with high spatial resolution and chemical or electronic structure contrast.[53−61] In this study, STXM was used to record images, elemental maps, and X-ray absorption near-edge structure (XANES) spectra to evaluate structure and morphology on the micrometer scale. Figure 8 shows a normal contrast image and C, O, and Nd elemental maps of a representative particle of Nd-BPP-7. XANES spectra obtained from this particle at the carbon and oxygen K-edges and Nd $M_{5,4}$-edges are provided in Figures S6−S8. The images in Figure 8 indicate that the sample was uniform in composition of C, O, and Nd at the nanometer scale.

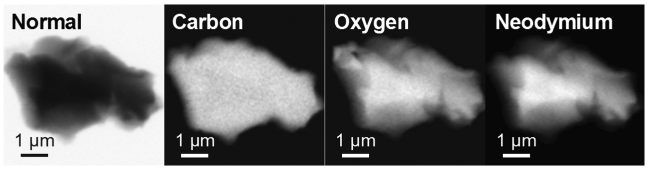

Figure 8. Four images of a representative particle from Nd-BPP-7 from which X-ray absorption spectra were collected: (from left to right) normal contrast image obtained with a photon energy of 960 eV; elemental map of carbon obtained by subtraction using photon energies of 280 and 300 eV with the regions containing C shown as white using a standard grayscale; elemental maps of oxygen and neodymium obtained by the same method using photon energies of 525 and 540 eV (O) and 960 and 980 eV (Nd).

To determine the efficiency of Nd binding by BPP-7, the Nd concentration relative to the C and O content in the PAF particle was evaluated using singular value decomposition (SVD) analysis, which has been established previously for a variety of environmental and geological materials.[62] The optical density of a target area in a given image is governed by OD = $\mu \times \rho \times t$, where μ is the mass absorption coefficient,[63] ρ is the density, and t is the sample thickness or path length. In this study, the intensity of the Nd M_5-edge step (μ) was proportional to the Nd concentration, [Nd], in the target area of a given particle. Similarly, the intensity of the edge step at the C or O K-edges was proportional to [C] and [O] in the same target area, respectively. Two values [Nd]/[C] and [Nd]/[O] were defined as the molar ratios of Nd and C or O in Nd-BPP-7. To provide an accurate measurement, analyses were conducted on more than 10 different target areas from several particles with approximately 10,000 total pixels, and errors are reported as the standard deviation from the multiple measurements. In this manner, the [Nd]/[C] molar ratio obtained was 0.011(3), which corresponds to 1.2(4) mmol of Nd per gram of BPP-7. The slightly lower Nd concentration relative to results from ICP-MS may reflect small inaccuracies of the theoretical values for the mass absorption coefficients,[63] or effects from surface contamination and saturation during the STXM measurement.

As described above, the EXAFS studies indicate that Nd is coordinated by two carboxylates in Nd-BPP-7. Hence, the uptake of Nd by BPP-7 can in this case be described by the following reaction, eq 1.

$$\begin{aligned} &C_{41}O_8H_{24} + Nd(ClO_4)_3 \\ &\quad \rightarrow (C_{41}O_8H_{22})Nd(ClO_4) + 2HClO_4 \end{aligned} \tag{1}$$

This stoichiometry affords a theoretical [Nd]/[O] molar ratio for the $(C_{41}O_8H_{24})Nd(ClO_4)$ product of 0.083. The significantly smaller experimental value of 0.027(5) reflects the presence of water molecules in the Nd coordination sphere. However, the exact number of water molecules could not be determined with confidence because of the possibility of incomplete $HClO_4$ removal following Nd adsorption.

Am^{3+} Adsorption. The final and arguably most challenging step in the separation of fission products is the separation of minor actinides from lanthanides (step C, Figure 1). Accordingly, Am^{3+} adsorption studies were also performed with BPP-7. Two sets of adsorption experiments were carried out to establish americium(III) ($^{243}Am^{3+}$) uptake in the material, and to evaluate the relative behavior of Nd^{3+} and Am^{3+} when interacting with BPP-7. Initially, the distribution coefficients of adsorption of Nd^{3+} and Am^{3+} were measured at varying pH and fixed concentration to evaluate the proton replacement ratios and coordination behavior of these species. Plots of the $\log(K_d)$ versus the measured pH for both metal ions are displayed in Figure 9. Both plots have a linearly increasing region, which corresponds to the equilibrium between protonated and deprotonated carboxylic acid groups, as determined by the concentrations of protons in solution. At pH > 3, the decrease in concentration of protons is likely not great enough to cause a change in the distribution of adsorbed metal ions. Therefore, $\log(K_d)$ shows no dependence upon pH in this region. In the pH-dependent region of the plot, the slope of the best-fit line corresponds to the proton replacement ratio, as determined from the balanced equation, eq 2, where n is the number of protons replaced per adsorbed metal ion.

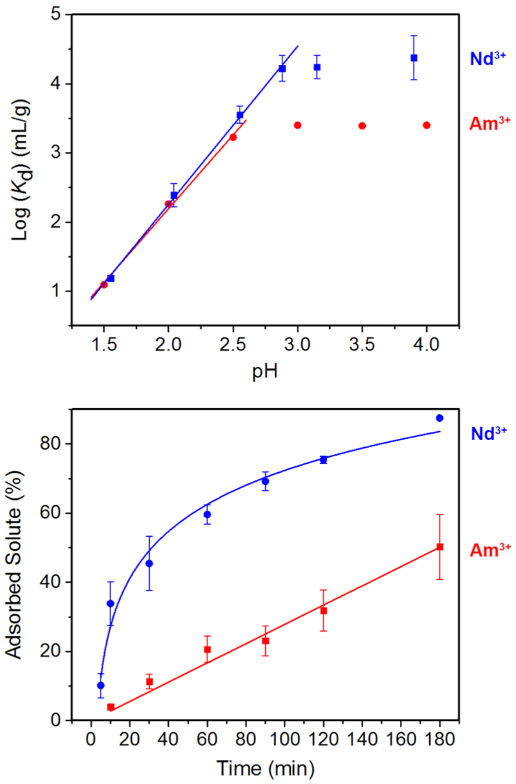

Figure 9. A plot of the log(K_d) versus measured pH for aqueous solutions containing Nd^{3+} and Am^{3+} ions (top), and kinetics for the uptake of Nd^{3+} and Am^{3+} (bottom).

$$n\mathrm{COOH} + \mathrm{M}^{x+} \rightarrow (\mathrm{COO})_n\mathrm{M} + n\mathrm{H}^+ \tag{2}$$

$$\log(K_d) \propto n(\mathrm{pH}) \tag{3}$$

The relationship between proton replacement ratio and log(K_d) is described with eq 3. The experimental proton replacement ratios for Nd^{3+} and Am^{3+} are $n = 2.29 \pm 0.06$ and 2.13 ± 0.12, respectively. These values are obtained from the slopes of the linear fit lines of the pH-dependent region in the pH versus log(K_d) plots. The experimental proton replacement ratio for Nd^{3+} adsorption validates the dual-site binding approximation made for Langmuir fitting of the Nd^{3+} adsorption isotherm. The experimental proton replacement ratio for Am^{3+} was slightly lower than that of Nd^{3+}, possibly due to its lower charge density, an effect previously established with Fe^{3+} and Sr^{2+} to a greater extent by IAST calculations. The lower charge density likely accounts for the lower maximum K_d value of Am^{3+} with respect to Nd^{3+}. In the high pH plateau region, the average observed K_d value is lower for Am^{3+} than Nd^{3+}, suggesting that the larger radius of Am^{3+} results in size exclusion and, hence, reduced adsorption by the framework. Thus, the maximum availability of sites for uptake is slightly lower for Am^{3+} adsorption than for Nd^{3+} adsorption. Despite these observations, the similarity between the derived proton replacement values for these species validates the choice of Nd^{3+} as an analogue for Am^{3+}.

Nd^{3+} Recovery. Two distinct postadsorption processes were investigated to evaluate their propensity for isolation or removal of adsorbed metal ions from Nd-BPP-7. To assess the feasibility of recovering the adsorbed metal by thermal decomposition of the framework, thermogravimetric analysis experiments were performed on BPP-7 and Nd-BPP-7, and the resulting combustion product was analyzed. The resulting data indicate near-complete combustion of the unloaded framework (<2% remaining) into volatile products (Figure 10). The postcombustion residue from Nd-BPP-7 is an oxide of Nd^{3+}, which is apparent from the presence of a slight digression in its combustion curve at ∼160 min. This suggests a phase change during the thermal decomposition of neodymium nitrate, corresponding to the formation of the intermediate product $NdO(NO_3)$, as previously proposed.[64] The near-complete decomposition of BPP-7 and isolation of the adsorbed metal ions in a dense oxide form illustrates a distinct advantage of employing porous aromatic frameworks as media for solution-based adsorption and subsequent removal of cationic nuclides.

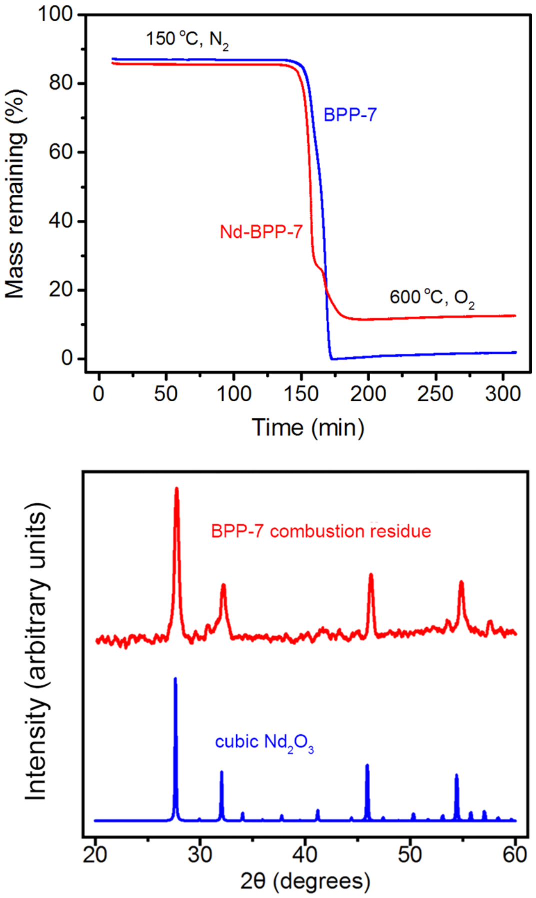

Figure 10. Top: Thermogravimetric analysis of Nd^{3+} adsorbed BBP-7 (red) and unloaded BBP-7 (blue). Both samples were treated identically, initially heated to 150 °C under an N_2 atmosphere for 150 min followed by a second heating to 600 °C under an O_2 atmosphere for another 150 min. Bottom: Powder X-ray diffraction patterns for the Nd-BPP-7 combustion product (red) and cubic Nd_2O_3 (blue).

The presence of neodymium oxide was investigated by powder X-ray diffraction on the residual combustion product of thermogravimetric analysis of Nd-BPP-7 (Figure 10) and was compared to the diffraction pattern of cubic Nd_2O_3 (blue).[65] The residue shows four diffraction peaks characteristic of cubic Nd_2O_3, suggesting that the Nd^{3+} was retained in the structure of the framework, and that the loaded framework may be thermally decomposed to yield the oxide form of the metal in crystalline form. The presence of Nd_2O_3 is further supported by the infrared spectrum of the neodymium-loaded combustion product (see Figure S9). Separation of solvated nuclear species into distinct solid forms is ideal for nuclear waste remediation and recyclability, as it maximizes the density of isotopes in the sample. Thus, this material has potential not only to separate particular components of a nuclear fuel but also to preserve them in a stable, solid, insoluble form. This solidification process is particularly important for fuel storage, as the long-term stability of a stored fuel is heavily dependent upon the nature of the solid, preventing leaching of contaminants over time, as well as reducing the potential for highly penetrating radiation to escape the containment vessel into the environment.[66] Industrial, large-scale processes are conducted as a covitrification with silica, which may cause separation of radionuclides and metallic phases, and poor solid phase stability.[67] However, the process described in our study allows for separation of nuclides prior to vitrification, with the added benefit of minimal contamination by the adsorbent, which can readily be discarded as volatile combustion products.

Desorption and Recyclability. The desorption of metal ions and recyclability of BPP-7 were also investigated by replacement of the adsorbed metal ions through reacidification of the framework with $HClO_4$. Following aqueous $HClO_4$ treatment, the adsorption isotherm of Nd^{3+} exhibited only a minimal (0.7%) decrease in uptake capacity compared to the freshly synthesized PAF (see Figure 11, top). Thus, not only is desorption of the loaded metal ions possible but the material may be reused for further separations. The recyclability of the framework was tested over five desorption/adsorption cycles at a single starting concentration (2.1 mM) (Figure 11, bottom). A near-constant decrease in uptake was observed for each adsorption/desorption cycle, resulting in a total decrease in adsorption from ~2 mmol/g to ~1.75 mmol/g after 5 recycling processes. These values suggest that approximately 20 iterations of BPP-7 recycling could be achieved before the material degrades to 50% capacity. The minimal loss of sorption capability may be attributed to deactivation of carboxylic acid functional groups, perhaps through decomposition of the framework by reaction with the strong acid. It is very likely that the regeneration conditions could be further optimized to improve recyclability.

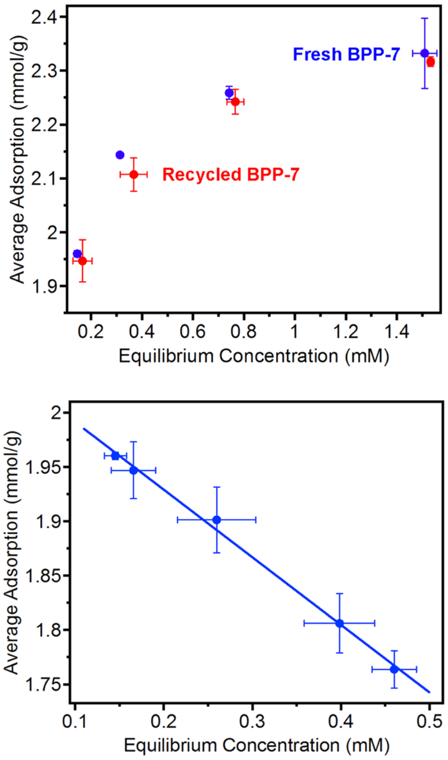

Figure 11. Recyclability of BPP-7 tested over 5 desorption/adsorption cycles at various equilibrium concentrations.

■ EXPERIMENTAL SECTION

General. The manipulations described below were performed primarily under aerobic conditions. BPP-7 was prepared according to a literature method[33] and desolvated under vacuum at 150 °C for 24 h prior to use. The compounds $Nd(NO_3)_3{\cdot}6H_2O$ (Sigma-Aldrich, 99.9%, Trace Metals Basis), $Sr(NO_3)_2$ (Alfa Aesar, 99.97%, Metals Basis), and $Fe(NO_3)_3{\cdot}9H_2O$ (Alfa Aesar, >98%, Metals Basis) were purchased from commercial vendors, and used as received. Arsenazo III (1,8-dihydroxynaphthalene-3,6-disulfonic acid-2,7-bis[(azo-2)-phenylarsonic acid]) was purchased from Aldrich, and used as received. A Varian Cary 5 UV−visible spectrophotometer was used for all absorbance measurements.

Metal Ion Adsorption Measurements Employing BPP-7. ***Nd.*** $Nd(NO_3)_3{\cdot}6H_2O$ (108.7 ± 0.25 mg) was dissolved in 250 mL of milli-Q water. From this stock solution, aliquots were directly added to the reaction mixtures to create solutions of concentrations of 20 μM to 1.0 mM.

Sr. $Sr(NO_3)_2$ (211.6 ± 0.3 mg) was dissolved in 20 mL of milli-Q water. From this stock solution, aliquots were directly added to the reaction mixtures to create solutions of concentrations 20 μm to 1.4 mM.

Fe. $Fe(NO_3)_3{\cdot}9H_2O$ (5049.6 ± 0.3 mg) was dissolved in 200 mL of milli-Q water. From this stock solution, aliquots were directly added to the reaction mixtures to create solutions of concentrations 23 μM to 0.77 mM.

To 1 mL of each of these metal nitrate batches, 1.525 ± 0.025 mg of BPP-7 was added and allowed to react on an orbital shaker for 48 h. Subsequently, the reaction mixtures were centrifuged to separate the metalated BPP-7 from solution, and the supernatant solutions were then titrated to pH 5 ± 0.5 with 0.1 N KOH. From these samples, aliquots were taken for UV−vis analysis and ICP-MS analysis, respectively.

Adsorption Isotherms of Nd(III), Fe(III), and Sr(II). Each data point of the isotherms corresponds to an independent adsorption experiment. The equilibrium concentrations of Nd(III) samples (high concentration, >2 mM), Sr(II), and Fe(III) were determined via UV−vis analysis. By contrast, the equilibrium concentrations of Nd(III) samples (<2 mM) were determined by ICP-MS. All data points from UV−vis were conducted in triplicate and the data points from ICP-MS analysis were performed in duplicate to estimate the standard error in the adsorption isotherm values.

To estimate selectivities, isotherm data were fitted with either a single- or dual-site Langmuir equation (eq 4), where n is the total amount adsorbed in mmol/g, C is the concentration in mM, $n_{sat,i}$ is the saturation capacity in mmol/g, and b_i is the Langmuir parameter in bar^{-1} for up to two sites, 1 and 2. The fitted parameters can be found in Table 1. Ideal adsorbed solution theory (IAST)[39] was then used to estimate the selectivity, S_{ads}, and amount of each component adsorbed for binary mixtures of Nd^{3+}/Fe^{3+}, Nd^{3+}/Sr^{2+}, and Fe^{3+}/Sr^{2+}. Note that the selectivity factor, S_{ads}, is defined according to eq 5, where n_i is the amount adsorbed of each component, as determined from IAST, and x_i is the mole fraction of each component in the solution phase at equilibrium.

$$n = \frac{n_{\mathrm{sat},1}b_1C}{1 + b_1C} + \frac{n_{\mathrm{sat},2}b_2C}{1 + b_2C} \quad (4)$$

$$S_{\mathrm{ads}} = \frac{n_1/n_2}{x_1/x_2} \quad (5)$$

Nd(III) Adsorption Kinetics and Proton Replacement. For the proton replacement reactions, 5 μM $Nd(NO_3)_3$ dissolved in water and combined with various concentrations (0.0001−0.032 M) of aqueous HNO_3 were allowed to react with BPP-7 for 24 h. The equilibrium concentrations of the solutions after separation from BPP-7 were measured by ICP-MS. The distribution coefficient, K_d, was calculated as described in eq 6, where C_0 and C_f are the initial and final metal ion concentrations in solution, respectively, V is the volume of the solution in mL, and M is the mass in grams of the adsorbent.

$$K_{\mathrm{d}} = \frac{C_{\mathrm{o}}/C_{\mathrm{f}}}{C_{\mathrm{f}}}\frac{V}{M} \quad (6)$$

Kinetics studies were performed with a 2 mM aqueous solution of $Nd(NO_3)_3$. Percent adsorption was calculated based upon the final and initial concentrations of $Nd(NO_3)_3$ in solution. All Nd(III) kinetics and proton replacement reactions were performed in duplicate.

Am(III) Adsorption Kinetics and Proton Replacement. Kinetics and proton replacement experiments for Am(III) were performed under the same conditions as the analogous Nd(III) reactions. Both adsorption experiments used 6 μM aqueous solutions of $^{243}Am(NO_3)_3$. The equilibrium concentration of Am(III) in solution was measured with liquid scintillation counting (LSC). The distribution coefficient was determined using eq 5.

UV−Visible Spectroscopic Analysis. Reaction solutions containing Nd(III) and Sr(II) ions were prepared for visible spectroscopy using arsenazo III. Specifically, a 760 μL aliquot of each reaction mixture was added to 200 μL of buffer solution, and 40 μL of 0.1% arsenazo III in water. Following a literature procedure,[68] the Nd(III)/arsenazo solution was fixed at pH 3 with a 0.1 M acetic acid buffer, while the Sr(II)/arsenazo solution was fixed at pH 8 with a 0.1 M HEPES buffer. The resulting metal−arsenazo complexes absorb at 653 and 647 nm, respectively, and extinction coefficients at these wavelengths were used to determine the concentration of Nd(III) and Sr(II) ions in solution via Beer's law. Extinction coefficients were determined using an appropriate calibration curve. The concentration of Fe(III) ions was determined in a similar manner using Beer's law and the direct absorbance of $Fe(NO_3)_3$ at 200 nm.

Recycling Experiment. BPP-7 was recycled by shaking for 12 h in 1 M $HClO_4$ to displace adsorbed metal ions, and then washing four times with tetrahydrofuran at 60 °C. The material was then dried by heating under vacuum at 150 °C for 24 h.

Physical Measurements. A PerkinElmer SCIEX Elan DRC II inductively coupled mass spectrometer within the Geochemistry Division at Lawrence Berkeley National Laboratory was used to determine the concentrations of Nd(III) samples at low concentrations (<2 mM). A Wallac 1414 liquid scintillation counter was used for liquid scintillation spectroscopy of all Am(III) samples. A 50 μL aliquot of each reaction solution was added to a scintillation vial containing 5 mL of MP Biomedicals EcoLumeTM liquid scintillation cocktail, and counted for 1 min. Thermogravimetric analyses of BPP-7 samples were carried out with a TA Instruments Q5000 TGA. The samples were heated to 150 °C under an N_2 atmosphere for 150 min, to remove any adsorbed solvents and gases, and were then heated to 600 °C under an O_2 atmosphere for 150 min. The Nd-loaded BPP-7 combustion product was characterized using a Bruker Advance D8 powder X-ray diffractometer. The simulated diffraction pattern was calculated from the crystallographic dimensions of cubic Nd_2O_3. Infrared spectra were collected with a PerkinElmer Advance Spectrum 400 FTIR spectrometer equipped with a Pike attenuated total reflectance accessory.

X-ray Absorption Fine Structure (XAFS). Near-edge and extended X-ray absorption fine structure (EXAFS) measurements were performed on BL11XU and BL14B1 at SPring-8. The operating energy and the ring current were 8 GeV and 99 mA in the topoff operation mode, respectively. The synchrotron radiation was monochromatized by liquid N_2 cooled Si(311) double crystal monochromators for the XAFS measurements. The optics and EXAFS measurement systems of BL11XU have been previously described.[69] Nd K-edge absorption spectra (43.569 keV) were collected in transmission using normal and quick monochromator scan mode (QXAFS mode) with Ar+N_2-filled ionization chambers at ambient pressure and temperature. Nd-BPP-7 powder was mixed with boron nitride powder and pressed to make a tablet with 1 mm thickness. Fifty scans were performed for the Nd-BPP-7 sample, and the spectra were averaged for the data analysis. EXAFS data analysis was performed according to a standard procedure using the program WinXAS (version 3.1).[70] Theoretical phases and amplitude required for the curve fitting were calculated by FEFF 8.2 code,[71] using the model information from refs 51 and 72. Details of the fitting procedure can be found in the Supporting Information.

Scanning Transmission X-ray Microscope (STXM)−X-ray Absorption Near Edge Structure Measurements. Data were collected using the STXM at the Advanced Light Source-Molecular Environmental Sciences (ALS-MES) elliptically polarizing undulator beamline 11.0.2, which is operated in topoff mode at 500 mA, in a ~0.5 atm He filled chamber.[73] Samples for STXM measurements were encapsulated between two 100 nm Si_3N_4 membranes (Silson). Energy calibrations were performed at the Ne K-edge for Ne (867.3 eV). The energy resolution (fwhm) was estimated at 0.2 eV, and spectra were collected using linearly polarized radiation. Spectra at each image pixel or particular regions of interest in the sample image were extracted from the "stack", which is a collection of images recorded at multiple, closely spaced photon energies across the absorption edge.[74−76] Standard data analysis procedures were followed, as described previously.[75,77−79]

The XAFS and STXM measurements were performed on BPP-7 samples that were exposed to Nd perchlorate solutions with low concentrations analogous to the nitrate solutions used for the adsorption determinations. At the low concentrations employed, the characteristics of weak perchlorate coordination are similar to those of nitrate.[80]

CONCLUSIONS

The foregoing results demonstrate the enormous potential of the interpenetrated porous aromatic framework BPP-7, which is densely functionalized with carboxylic acid binding groups, for lanthanide and actinide group separation, as needed for the treatment of fission products. Significantly, BPP-7 exhibits a high selectivity for the uptake of neodymium in the presence of strontium and iron. Particularly important is the preferential binding of neodymium at low concentrations compared to iron, which represents a realistic scenario in the waste mixture, where the corrosion of stainless steel from tanks and iron-containing reagents would deliver metal ions such as iron in much higher concentrations. Adsorption of the ions was evaluated by the Langmuir model, which required including both a strong and a weak adsorption site for Nd^{3+} and Sr^{2+}, while the Fe^{3+} data could be modeled with only one weak site. The stronger binding for Sr^{2+} and particularly for Nd^{3+} is ascribed to an appropriately sized binding pocket featuring multiple carboxylic acid groups. Further encouraging the use of BPP-7 for the purpose of lanthanide/actinide group separation is the excellent recyclability and combustibility of BPP-7. Tests have shown that desorption of BPP-7 to recover the loaded metal ions is possible, and that subsequent reuse of the material for further metal ion uptake shows only minor decrease in adsorption capacity.

■ ASSOCIATED CONTENT

Ⓢ Supporting Information

The Supporting Information is available free of charge on the ACS Publications website at DOI: 10.1021/acscentsci.6b00066.

IAST selectivities and purities for binary mixtures, XAFS fitting details, carbon/oxygen/Nd $M_{5,4}$ edges, infrared spectra, and uptake of recycled BPP-7 (PDF)

■ AUTHOR INFORMATION

Corresponding Author

*E-mail: jrlong@berkeley.edu.

Present Addresses

[‖]J.F.V.H.: Massachusetts Institute of Technology, 77 Massachusetts Ave., Cambridge, MA 02139.

[#]S.W.: School of Radiation Medicine and Protection (SRMP) and School of Radiological and Interdisciplinary Sciences (RAD-X), Soochow University, Suzhou, Jiangsu 215123, China.

Author Contributions

[§]S.D. and N.K.B. contributed equally.

Notes

The authors declare no competing financial interest.

■ ACKNOWLEDGMENTS

Measurement of metal ion uptake in BPP-7 and characterization of the resulting materials were supported by the Director, Office of Science, Office of Basic Energy Sciences, Division of Chemical Sciences, Geosciences, and Biosciences Heavy Element Chemistry Program of the U.S. Department of Energy at Lawrence Berkeley National Laboratory under Contract No. DE-AC02-05CH11231. The synthesis of BPP-7 and analysis of its metal ion adsorption behavior were supported through the Center for Gas Separations Relevant to Clean Energy Technologies, an Energy Frontier Research Center funded by the U.S. Department of Energy, Office of Science, Office of Basic Energy Sciences under Award DE-SC0001015. S.W. was supported by the Laboratory Directed Research and Development Program at LBNL. Work at the MES Beamline 11.0.2 was supported by the Director, Office of Science, Office of Basic Energy Sciences, Division of Chemical Sciences, Geosciences, and Biosciences Condensed Phase and Interfacial Molecular Sciences Program of the U.S. Department of Energy at Lawrence Berkeley National Laboratory under Contract No. DE-AC02-05CH11231. The Advanced Light Source and TT were supported by the Director, Office of Science, Office of Basic Energy Sciences, of the U.S. Department of Energy under Contract No. DE-AC02-05CH11231. The synchrotron radiation XAFS experiments were performed at the BL11XU and BL14B1 of SPring-8 with the approval of the Japan Synchrotron Radiation Research Institute (JASRI) (Proposal Nos. 2013B3504, 2013B3613, and 2012B3613).

■ REFERENCES

(1) Carbol, P.; Wegen, D. H.; Wiss, T.; Fors, P. Spent Fuel as Waste Material. In *Comprehensive Nuclear Materials*; Rudy, J. M. K., Ed.; Elsevier: Oxford, 2012; Vol. *5*, pp 389−420.

(2) Ehrnstén, U. Corrosion and Stress Corrosion Cracking of Austenitic Stainless Steels. In *Comprehensive Nuclear Materials*; Rudy, J. M. K., Ed.; Elsevier: Oxford, 2012; Vol. *5*, pp 93−104.

(3) Glatz, J. P. Spent Fuel Dissolution and Reprocessing Processes. In *Comprehensive Nuclear Materials*; Rudy, J. M. K., Ed.; Elsevier: Oxford, 2012; Vol. *5*, pp 343−366.

(4) Anderson, H. H.; Asprey, L. B. Solvent Extraction Process for Plutonium. US292406 A, May 8, 1947.

(5) Kumari, N.; Pathak, P. N.; Prabhu, D. R.; Manchanda, V. K. Comparison of Extraction Behavior of Neptunium from Nitric Acid Medium Employing Tri-n-Butyl Phosphate and N,N-dihexyl Octanamide as Extractants. *Sep. Sci. Technol.* **2012**, *47*, 1492−1497.

(6) Salvatores, M.; Palmiotti, G. Radioactive Waste Partitioning and Transmutation within Advanced Fuel Cycles: Achievements and Challenges. *Prog. Part. Nucl. Phys.* **2011**, *66*, 144−166.

(7) Magill, J.; Berthou, V.; Haas, D.; Galy, J.; Schenkel, R.; Wiese, H. W.; Heusener, G.; Tommasi, J.; Youinou, G. Impact Limits of Partitioning and Transmutation Scenarios on the Radiotoxicity of Actinides in Radioactive Waste. *Nucl. Energy* **2003**, *42*, 263−277.

(8) Sasaki, Y.; Tachimori, S. Extraction of Actinides(III), (IV), (V), (VI), and Lanthanides(III) by Structurally Tailored Diamides. *Solvent Extr. Ion Exch.* **2002**, *20*, 21−34.

(9) Sasaki, Y.; Sugo, Y.; Suzuki, S.; Tachimori, S. The Novel Extractants, Diglycoamides, for the Extraction of Lanthanides and Actinides in HNO_3-n-Dodecane System. *Solvent Extr. Ion Exch.* **2001**, *19*, 91−103.

(10) Schulz, W. W.; Horwitz, E. P. The Truex Process and the Management of Liquid Tru Uwaste. *Sep. Sci. Technol.* **1988**, *23*, 1191−1210.

(11) Philip Horwitz, E.; Kalina, D. C.; Diamond, H.; Vandegrift, G. F.; Schulz, W. W. The TRUEX Process - A Process for the Extraction of the Transuranic Elements from Nitric AC in Wastes Utilizing Modified PUREX Solvent. *Solvent Extr. Ion Exch.* **1985**, *3*, 75−109.

(12) Panak, P. J.; Geist, A. Complexation and Extraction of Trivalent Actinides and Lanthanides by Triazinylpyridine N-Donor Ligands. *Chem. Rev.* **2013**, *113*, 1199−1236.

(13) Peterman Dean, R.; Law Jack, D.; Todd Terry, A.; Tillotson Richard, D. Use of Cyanex-301 for Separation of Am/Cm from Lanthanides in an Advanced Nuclear Fuel Cycle. In *Separations for the Nuclear Fuel Cycle in the 21st Century*; ACS Symposium Series; American Chemical Society: Washington, DC, 2006; Vol. *933*, pp 251−259.

(14) Tranter, T. J. *Solid-phase Extraction Technology for Actinide and Lanthanide Separations in Nuclear Fuel Reprocessing*; Woodhead Publishing: Cambridge, 2011.

(15) Ling, L.; Zhang, W.-x. Enrichment and Encapsulation of Uranium with Iron Nanoparticle. *J. Am. Chem. Soc.* **2015**, *137*, 2788−2791.

(16) Makowski, P.; Deschanels, X.; Grandjean, A.; Meyer, D.; Toquer, G.; Goettmann, F. Mesoporous Materials in the Field of

Nuclear Industry: Applications and Perspectives. *New J. Chem.* **2012**, *36*, 531−541.

(17) Batuk, O. N.; Szabo, V. D.; Denecke, M. A.; Vitova, T.; Kalmykov, S. N. Synthesis and Characterization of Thorium, Uranium and Cerium Oxide Nanoparticles. *Radiochim. Acta* **2013**, *101*, 233.

(18) Zhang, A.; Wei, Y.; Hoshi, H.; Kumagai, M.; Kamiya, M.; Koyama, T. Resistance Properties of a Macroporous Silica-based N,N,N′,N′-tetraoctyl-3-oxapentane-1,5-diamide-impregnated Polymeric Adsorption Material against Nitric Acid, Temperature and γ-Irradiation. *Radiat. Phys. Chem.* **2005**, *72*, 669−678.

(19) Zhang, A.; Wei, Y.; Kumagai, M.; Koma, Y.; Koyama, T. Resistant Behavior of a Novel Silica-based Octyl(phenyl)-N,N-diisobutyl Carbamoylmethylphoshine Oxide Neutral Extraction Resin against Nitric Acid, Temperature and γ-Radiation. *Radiat. Phys. Chem.* **2005**, *72*, 455−463.

(20) O'Keeffe, M.; Yaghi, O. M. Deconstructing the Crystal Structures of Metal-Organic Frameworks and Related Materials into Their Underlying Nets. *Chem. Rev.* **2012**, *112*, 675−702.

(21) Getman, R. B.; Bae, Y.-S.; Wilmer, C. E.; Snurr, R. Q. Review and Analysis of Molecular Simulations of Methane, Hydrogen, and Acetylene Storage in Metal-Organic Frameworks. *Chem. Rev.* **2012**, *112*, 703−723.

(22) Sumida, K.; Rogow, D. L.; Mason, J. A.; McDonald, T. M.; Bloch, E. D.; Herm, Z. R.; Bae, T.-H.; Long, J. R. Carbon Dioxide Capture in Metal−Organic Frameworks. *Chem. Rev.* **2012**, *112*, 724−781.

(23) Suh, M. P.; Park, H. J.; Prasad, T. K.; Lim, D.-W. Hydrogen Storage in Metal−Organic Frameworks. *Chem. Rev.* **2012**, *112*, 782−835.

(24) Wu, H.; Gong, Q.; Olson, D. H.; Li, J. Commensurate Adsorption of Hydrocarbons and Alcohols in Microporous Metal-Organic Frameworks. *Chem. Rev.* **2012**, *112*, 836−868.

(25) Yanai, N.; Kitayama, K.; Hijikata, Y.; Sato, H.; Matsuda, R.; Kubota, Y.; Takata, M.; Mizuno, M.; Uemura, T.; Kitagawa, S. Gas Detection by Structural Variations of Fluorescent Guest Molecules in a Flexible Porous Coordination Polymer. *Nat. Mater.* **2011**, *10*, 787−793.

(26) Wang, C.; Xie, Z.; deKrafft, K. E.; Lin, W. Doping Metal−Organic Frameworks for Water Oxidation, Carbon Dioxide Reduction, and Organic Photocatalysis. *J. Am. Chem. Soc.* **2011**, *133*, 13445−13454.

(27) Li, J.-R.; Sculley, J.; Zhou, H.-C. Metal−Organic Frameworks for Separations. *Chem. Rev.* **2012**, *112*, 869−932.

(28) Carboni, M.; Abney, C. W.; Liu, S.; Lin, W. Highly Porous and Stable Metal-Organic Frameworks for Uranium Extraction. *Chem. Sci.* **2013**, *4*, 2396−2402.

(29) Ben, T.; Ren, H.; Ma, S.; Cao, D.; Lan, J.; Jing, X.; Wang, W.; Xu, J.; Deng, F.; Simmons, J. M.; Qiu, S.; Zhu, G. Targeted Synthesis of a Porous Aromatic Framework with High Stability and Exceptionally High Surface Area. *Angew. Chem., Int. Ed.* **2009**, *48*, 9457−9460.

(30) Lu, W.; Yuan, D.; Sculley, J.; Zhao, D.; Krishna, R.; Zhou, H.-C. Sulfonate-Grafted Porous Polymer Networks for Preferential CO_2 Adsorption at Low Pressure. *J. Am. Chem. Soc.* **2011**, *133*, 18126.

(31) Lu, W.; Sculley, J. P.; Yuan, D.; Krishna, R.; Wei, Z.; Zhou, H.-C. Polyamine-Tethered Porous Polymer Networks for Carbon Dioxide Capture from Flue Gas. *Angew. Chem., Int. Ed.* **2012**, *51*, 7480−7484.

(32) Additional stability observations, especially in the presence of strong base, have also been made in our laboratory.

(33) Van Humbeck, J. F.; McDonald, T. M.; Jing, X.; Wiers, B. M.; Zhu, G.; Long, J. R. Ammonia Capture in Porous Organic Polymers Densely Functionalized with Brønsted Acid Groups. *J. Am. Chem. Soc.* **2014**, *136*, 2432−2440.

(34) The illustration in Figure 3 is meant to illustrate multifold interpenetration (>2-fold) rather than precise and uniform 3-fold interpenetration.

(35) For simplicity, we will designate metal ion binding to the surfaces within the porous carboxylic acid functionalized materials discussed throughout this article as corresponding to "adsorption". It is important to note, however, that the metal ion binding phenomenon in these materials will generally not just involve interactions with the carboxylic acid groups, but may also involve some degree of ion exchange to release protons and afford metal−carboxylate interactions.

(36) Centi, G.; Joester, D. Nuclear Energy: A Perspective on Recent Results on the Removal of Strontium from Waste. *ChemSusChem* **2011**, *4*, 419−420.

(37) Zhang, W.; He, X.; Ye, G.; Yi, R.; Chen, J. Americium(III) Capture Using Phosphonic Acid-Functionalized Silicas with Different Mesoporous Morphologies: Adsorption Behavior Study and Mechanism Investigation by EXAFS/XPS. *Environ. Sci. Technol.* **2014**, *48*, 6874−6881.

(38) Yabutani, T.; Sumi, H.; Nakamura, T.; Akatsuki, S.; Thuy, L. T. X. Multielemental Elution Behavior of Metal Ions Adsorbed on Iminodiacetic Acid Chelating Resin by Using Hydrogen Peroxide as an Eluent. *Anal. Sci.* **2012**, *28*, 463−468.

(39) Myers, A. L.; Prausnitz, J. M. Thermodynamics of Mixed-gas Adsorption. *AIChE J.* **1965**, *11*, 121−127.

(40) Al-Asheh, S.; Banat, F.; Al-Omari, R.; Duvnjak, Z. Predictions of Binary Sorption Isotherms for the Sorption of Heavy Metals by Pine Bark Using Single Isotherm Data. *Chemosphere* **2000**, *41*, 659−665.

(41) Papageorgiou, S. K.; Katsaros, F. K.; Kouvelos, E. P.; Kanellopoulos, N. K. Prediction of Binary Adsorption Isotherms of Cu^{2+}, Cd^{2+} and Pb^{2+} on Calcium Alginate Beads from Single Adsorption Data. *J. Hazard. Mater.* **2009**, *162*, 1347−1354.

(42) Krishna, R.; van Baten, J. M. Using Molecular Simulations for Screening of Zeolites for Separation of CO_2/CH_4 Mixtures. *Chem. Eng. J.* **2007**, *133*, 121−131.

(43) Krishna, R.; Smit, B.; Calero, S. Entropy Effects During Sorption of Alkanes in Zeolites. *Chem. Soc. Rev.* **2002**, *31*, 185−194.

(44) Peng, X.; Cheng, X.; Cao, D. Computer Simulations for the Adsorption and Separation of $CO_2/CH_4/H_2/N_2$ Gases by UMCM-1 and UMCM-2 Metal-Organic Frameworks. *J. Mater. Chem.* **2011**, *21*, 11259−11270.

(45) Mason, J. A.; Sumida, K.; Herm, Z. R.; Krishna, R.; Long, J. R. Evaluating Metal-organic Frameworks for Post-combustion Carbon Dioxide Capture via Temperature Swing Adsorption. *Energy Environ. Sci.* **2011**, *4*, 3030−3040.

(46) Burcl, R. Strategy and Methodology for Radioactive Waste Characterization. International Atomic Energy Agency. In *Strategy and Methodology for Radioactive Waste Characterization. International Atomic Energy Agency*; International Atomic Energy Agency: Austria, 2007; pp 1−169.

(47) Edelstein, N. M.; Fuger, J.; Katz, J. J.; Morss, L. R. Summary and Comparison of Properties of the Actinide and Transactinide Elements. In *The Chemistry of the Actinide and Transactinide Elements*; Morss, L. R., Edelstein, N. M., Fuger, J., Eds.; Springer: Dordrecht, The Netherlands, 2010; Vol. 3.

(48) David, F. H.; Fourest, B. Structure of Trivalent Lanthanide and Actinide Aquo Ions. *New J. Chem.* **1997**, *21*, 167.

(49) Yaita, T.; Narita, H.; Suzuki, S.; Tachimori, S.; Motohashi, H.; Shiwaku, H. Structural Study of Lanthanides(III) in Aqueous Nitrate and Chloride Solutions by EXAFS. *J. Radioanal. Nucl. Chem.* **1999**, *239*, 371−375.

(50) Mondry, A.; Starynowicz, P. Crystal Structure and Absorption Spectroscopy of a Neodymium(III) Complex with Triethylenetetraaminehexaacetic Acid, $Na_3[Nd(TTHA)]\cdot 2.5NaClO_4\cdot 7.617H_2O$. *Inorg. Chem.* **1997**, *36*, 1176−1180.

(51) Tang, X.; Yue, S.; Li, P.; Wang, N.; Liu, Y. Hydrothermal Synthesis and Crystal Structure Study of Two Novel 3-D Mellitates $\{Nd_2[C_6(COO)_6](H_2O)_6\}$ and $\{Ho_2[C_6(COO)_6](H_2O)_6\}$. *J. Rare Earths* **2008**, *26*, 800−803.

(52) Huskowska, E.; Legendziewicz, J.; Schleid, T.; Meyer, G. A Special Double Issue Devoted to the Workshop on the Basic and Applied Aspects of Rare Earths do the Lanthanides Form Inner Sphere Complexes with ClO_4^- Ions in Competition with H_2O Molecules? *Mater. Chem. Phys.* **1992**, *31*, 117−122.

(53) Cosmidis, J.; Benzerara, K.; Nassif, N.; Tyliszczak, T.; Bourdelle, F. Characterization of Ca-phosphate Biological Materials by Scanning

Transmission X-ray Microscopy (STXM) at the Ca L 2,3 -, P L 2,3 -and C K- Edges. *Acta Biomater.* **2015**, *12*, 260−269.

(54) Shapiro, D. A.; Yu, Y.-S.; Tyliszczak, T.; Cabana, J.; Celestre, R.; Chao, W.; Kaznatcheev, K.; Kilcoyne, A. L. D.; Maia, F.; Marchesini, S.; Meng, Y. S.; Warwick, T.; Yang, L. L.; Padmore, H. A. Chemical Composition Mapping with Nanometre Resolution by Soft X-ray Microscopy. *Nat. Photonics* **2014**, *8*, 765−769.

(55) Kaulich, B.; Thibault, P.; Gianoncelli, A.; Kiskinova, M. Transmission and Emission X-ray Microscopy: Operation Modes, Contrast Mechanisms and Applications. *J. Phys.: Condens. Matter* **2011**, *23*, 083002−083025.

(56) Yang, Y.; Saiers, J. E.; Xu, N.; Minasian, S. G.; Tyliszczak, T.; Kozimor, S. A.; Shuh, D. K.; Barnett, M. O. Impact of Natural Organic Matter on Uranium Transport through Saturated Geologic Materials: From Molecular to Column Scale. *Environ. Sci. Technol.* **2012**, *46*, 5931−5938.

(57) Brownlee, D.; Tsou, P.; Aleon, J.; Alexander, C. M. O. D.; Araki, T.; Bajt, S.; Baratta, G. A.; Bastien, R.; Bland, P.; Bleuet, P.; Borg, J.; Bradley, J. P.; Brearley, A.; Brenker, F.; Brennan, S.; Bridges, J. C.; Browning, N. D.; Brucato, J. R.; Bullock, E.; Burchell, M. J.; Busemann, H.; Butterworth, A.; Chaussidon, M.; Cheuvront, A.; Chi, M.; Cintala, M. J.; Clark, B. C.; Clemett, S. J.; Cody, G.; Colangeli, L.; Cooper, G.; Cordier, P.; Daghlian, C.; Dai, Z.; D'Hendecourt, L.; Djouadi, Z.; Dominguez, G.; Duxbury, T.; Dworkin, J. P.; Ebel, D. S.; Economou, T. E.; Fakra, S.; Fairey, S. A. J.; Fallon, S.; Ferrini, G.; Ferroir, T.; Fleckenstein, H.; Floss, C.; Flynn, G.; Franchi, I. A.; Fries, M.; Gainsforth, Z.; Gallien, J. P.; Genge, M.; Gilles, M. K.; Gillet, P.; Gilmour, J.; Glavin, D. P.; Gounelle, M.; Grady, M. M.; Graham, G. A.; Grant, P. G.; Green, S. F.; Grossemy, F.; Grossman, L.; Grossman, J. N.; Guan, Y.; Hagiya, K.; Harvey, R.; Heck, P.; Herzog, G. F.; Hoppe, P.; Hoerz, F.; Huth, J.; Hutcheon, I. D.; Ignatyev, K.; Ishii, H.; Ito, M.; Jacob, D.; Jacobsen, C.; Jacobsen, S.; Jones, S.; Joswiak, D.; Jurewicz, A.; Kearsley, A. T.; Keller, L. P.; Khodja, H.; Kilcoyne, A. L. D.; Kissel, J.; Krot, A.; Langenhorst, F.; Lanzirotti, A.; Le, L.; Leshin, L. A.; Leitner, J.; Lemelle, L.; Leroux, H.; Liu, M.-C.; Luening, K.; Lyon, I.; MacPherson, G.; Marcus, M. A.; Marhas, K.; Marty, B.; Matrajt, G.; McKeegan, K.; Meibom, A.; Mennella, V.; Messenger, K.; Messenger, S.; Mikouchi, T.; Mostefaoui, S.; Nakamura, T.; Nakano, T.; Newville, M.; Nittler, L. R.; Ohnishi, I.; Ohsumi, K.; Okudaira, K.; Papanastassiou, D. A.; Palma, R.; Palumbo, M. E.; Pepin, R. O.; Perkins, D.; Perronnet, M.; Pianetta, P.; Rao, W.; Rietmeijer, F. J. M.; Robert, F.; Rost, D.; Rotundi, A.; Ryan, R.; Sandford, S. A.; Schwandt, C. S.; See, T. H.; Schlutter, D.; Sheffield-Parker, J.; Simionovici, A.; Simon, S.; Sitnitsky, I.; Snead, C. J.; Spencer, M. K.; Stadermann, F. J.; Steele, A.; Stephan, T.; Stroud, R.; Susini, J.; Sutton, S. R.; Suzuki, Y.; Taheri, M.; Taylor, S.; Teslich, N.; Tomeoka, K.; Tomioka, N.; Toppani, A.; Trigo-Rodriguez, J. M.; Troadec, D.; Tsuchiyama, A.; Tuzzolino, A. J.; Tyliszczak, T.; Uesugi, K.; Velbel, M.; Vellenga, J.; Vicenzi, E.; Vincze, L.; Warren, J.; Weber, I.; Weisberg, M.; Westphal, A. J.; Wirick, S.; Wooden, D.; Wopenka, B.; Wozniakiewicz, P.; Wright, I.; Yabuta, H.; Yano, H.; Young, E. D.; Zare, R. N.; Zega, T.; Ziegler, K.; Zimmerman, L.; Zinner, E.; Zolensky, M. Research Aticle - Comet 81P/Wild 2 Under a Microscope. *Science* **2006**, *314*, 1711−1716.

(58) Cody, G. D.; Ade, H.; Alexander, C. M. O. D.; Araki, T.; Butterworth, A.; Fleckenstein, H.; Flynn, G.; Gilles, M. K.; Jacobsen, C.; Kilcoyne, A. L. D.; Messenger, K.; Sandford, S. A.; Tyliszczak, T.; Westphal, A. J.; Wirick, S.; Yabuta, H. Quantitative Organic and Light-element Analysis of Comet 81P/Wild 2 Particles Using C-, N-, and O-mu-XANES. *Meteorit. Planet. Sci.* **2008**, *43*, 353−365.

(59) Dynes, J. J.; Tyliszczak, T.; Araki, T.; Lawrence, J. R.; Swerhone, G. D. W.; Leppard, G. G.; Hitchcock, A. P. Speciation and Quantitative Mapping of Metal Species in Microbial Biofilms using Scanning Transmission X-ray Microscopy. *Environ. Sci. Technol.* **2006**, *40*, 1556−1565.

(60) Lawrence, J. R.; Swerhone, G. D. W.; Leppard, G. G.; Araki, T.; Zhang, X.; West, M. M.; Hitchcock, A. P. Scanning Transmission X-ray, Laser Scanning, and Transmission Electron Microscopy Mapping of the Exopolymeric Matrix of Microbial Biofilms. *Appl. Environ. Microb.* **2003**, *69*, 5543−5554.

(61) Urquhart, S. G.; Hitchcock, A. P.; Smith, A. P.; Ade, H. W.; Lidy, W.; Rightor, E. G.; Mitchell, G. E. NEXAFS Spectromicroscopy of Polymers: Overview and Quantitative Analysis of Polyurethane Polymers. *J. Electron Spectrosc. Relat. Phenom.* **1999**, *100*, 119−135.

(62) Koprinarov, I. N.; Hitchcock, A. P.; McCrory, C. T.; Childs, R. F. Quantitative Mapping of Structured Polymeric Systems Using Singular Value Decomposition Analysis of Soft X-ray Images. *J. Phys. Chem. B* **2002**, *106*, 5358−5364.

(63) Chantler, C. T. Detailed Tabulation of Atomic Form Factors, Photoelectric Absorption and Scattering Cross Section, and Mass Attenuation Coefficients in the Vicinity of Absorption Edges in the Soft X-Ray (Z = 30−36, Z = 60−89, E = 0.1 keV−10 keV), Addressing Convergence Issues of Earlier Work. *J. Phys. Chem. Ref. Data* **2000**, *29*, 597−1056.

(64) Van Vuuren, C. P. J.; Strydom, C. A. The Thermal Decomposition of Neodymium Nitrate. *Thermochim. Acta* **1986**, *104*, 293−298.

(65) Hirosaki, N.; Ogata, S.; Kocer, C. Ab Initio Calculation of the Crystal Structure of the Lanthanide Ln_2O_3 Sesquioxides. *J. Alloys Compd.* **2003**, *351*, 31−34.

(66) Wu, L.; Liu, N.; Qin, Z.; Shoesmith, D. W. Modeling the Radiolytic Corrosion of Fractured Nuclear Fuel under Permanent Disposal Conditions. *J. Electrochem. Soc.* **2014**, *161*, E3259−E3266.

(67) West Valley Demonstration Project: Draft Waste-Incidental-to-Reprocessing Evaluation for the Concentrator Feed Makeup Tank and the Meter Feed Hold Tank. In *West Valley Demonstration Project: Draft Waste-Incidental-to-Reprocessing Evaluation for the Concentrator Feed Makeup Tank and the Meter Feed Hold Tank*; U.S. Department of Energy: West Valley, NY, 2012; p 1.

(68) Hosten, E.; Rohwer, H. Interaction of Anions with Arsenazo III-lanthanide (III) Complexes. *Anal. Chim. Acta* **1997**, *345*, 227−233.

(69) Shiwaku, H.; Mitsui, T.; Tozawa, K.; Kiriyama, K.; Harami, T.; Mochozuki, T. Cryogenically Cooled Monochromator with Multi-crystal Switching System on BL11XU at SPring-8. *AIP Conf. Proc.* **2004**, *705*, 659.

(70) Ressler, T. WinXAS: a Program for X-ray Absorption Spectroscopy Data Analysis under MS-Windows. *J. Synchrotron Radiat.* **1998**, *5*, 118−122.

(71) Ankudinov, A. L.; Rehr, J. J. Theory of Solid-state Contributions to the X-ray Elastic Scattering Amplitude. *Phys. Rev. B: Condens. Matter Mater. Phys.* **2000**, *62*, 2437−2445.

(72) Schauer, C. K.; Anderson, O. P. Highly polydentate ligands. Part 4. Crystal Structures of Neodymium(III) and Erbium(III) Complexes of 3,12-bis(carboxymethyl)-6,9-dioxa-3,12-diazatetradecanedioate(4-). *J. Chem. Soc., Dalton Trans.* **1989**, 185−191.

(73) Bluhm, H.; Andersson, K.; Araki, T.; Benzerara, K.; Brown, G. E.; Dynes, J. J.; Ghosal, S.; Gilles, M. K.; Hansen, H. C.; Hemminger, J. C.; Hitchcock, A. P.; Ketteler, G.; Kilcoyne, A. L. D.; Kneedler, E.; Lawrence, J. R.; Leppard, G. G.; Majzlam, J.; Mun, B. S.; Myneni, S. C. B.; Nilsson, A.; Ogasawara, H.; Ogletree, D. F.; Pecher, K.; Salmeron, M.; Shuh, D. K.; Tonner, B.; Tyliszczak, T.; Warwick, T.; Yoon, T. H. Soft X-ray Microscopy and Spectroscopy at the Molecular Environmental Science Beamline at the Advanced Light Source. *J. Electron Spectrosc. Relat. Phenom.* **2006**, *150*, 86−104.

(74) Gianetti, T. L.; Nocton, G.; Minasian, S. G.; Tomson, N. C.; Kilcoyne, A. L. D.; Kozimor, S. A.; Shuh, D. K.; Tyliszczak, T.; Bergman, R. G.; Arnold, J. Diniobium Inverted Sandwich Complexes with μ-η^6:η^6-Arene Ligands: Synthesis, Kinetics of Formation, and Electronic Structure. *J. Am. Chem. Soc.* **2013**, *135*, 3224−3236.

(75) Minasian, S. G.; Keith, J. M.; Batista, E. R.; Boland, K. S.; Bradley, J. A.; Daly, S. R.; Sokaras, D.; Kozimor, S. A.; Lukens, W. W.; Martin, R. L.; Nordlund, D.; Seidler, G. T.; Shuh, D. K.; Tyliszczak, T.; Wagner, G. L.; Weng, T. C.; Yang, P. Covalency in Metal-Oxygen Multiple Bonds Evaluated Using Oxygen K-edge Spectroscopy and Electronic Structure Theory. *J. Am. Chem. Soc.* **2013**, *135*, 1864−1871.

(76) Minasian, S. G.; Keith, J. M.; Batista, E. R.; Boland, K. S.; Kozimor, S. A.; Martin, R. L.; Shuh, D. K.; Tyliszczak, T.; Vernon, L. J. Carbon K-Edge X-ray Absorption Spectroscopy and Time-Dependent

Density Functional Theory Examination of Metal−Carbon Bonding in Metallocene Dichlorides. *J. Am. Chem. Soc.* **2013**, *135*, 14731−14740.

(77) Minasian, S. G.; Krinsky, J. L.; Rinehart, J. D.; Copping, R.; Tyliszczak, T.; Janousch, M.; Shuh, D. K.; Arnold, J. A Comparison of 4f vs 5f Metal-Metal Bonds in $(CpSiMe_3)_3$M-ECp* (M = Nd, U; E = Al, Ga; Cp* = C_5Me_5): Synthesis, Thermodynamics, Magnetism, and Electronic Structure. *J. Am. Chem. Soc.* **2009**, *131*, 13767−13783.

(78) Bugaris, D. E.; Copping, R.; Tyliszczak, T.; Shuh, D. K.; Ibers, J. A. $La_2U_2Se_9$: An Ordered Lanthanide/Actinide Chalcogenide with a Novel Structure Type. *Inorg. Chem.* **2010**, *49*, 2568−2575.

(79) Bugaris, D. E.; Choi, E. S.; Copping, R.; Glans, P.-A.; Minasian, S. G.; Tyliszczak, T.; Kozimor, S. A.; Shuh, D. K.; Ibers, J. A. Pentavalent and Tetravalent Uranium Selenides, $Tl_3Cu_4USe_6$ and $Tl_2Ag_2USe_4$: Syntheses, Characterization, and Structural Comparison to Other Layered Actinide Chalcogenide Compounds. *Inorg. Chem.* **2011**, *50*, 6656−6666.

(80) Csoregh, I.; Huskowska, E.; Ertan, A.; Legendziewicz, J.; Kierkegaard, P. Crystal Structure of a Novel Neodymium Hydroxide Perchlorate Hydrate, $Nd_2(OH)_3(ClO_4)3.5H_2O$. *Acta Chem. Scand.* **1989**, *43*, 829−833.